The absence of an effect of nickel on iron isotope fractionation during core formation

E. Kubik, P. A. Sossi, J. Siebert, E. Inglis, M. Roskosz, E. Siciliano Rego, N. Wehr, F. Moynier

The absence of an effect of nickel on iron isotope fractionation during core formation

E. Kubik[1], P.A. Sossi[1,2], J. Siebert[1,3], E. Inglis[1], M. Roskosz[4], E. Siciliano Rego[1,5,6], N. Wehr[1], F. Moynier[1].

[1]Université de Paris, Institut de Physique du Globe de Paris, CNRS, UMR 7154, 1 Rue Jussieu, 75005 Paris, France

[2]Institute of Geochemistry and Petrology, ETH Zürich, CH-8092 Zürich, Switzerland

[3]Institut Universitaire de France, Paris, France

[4]Institut de Minéralogie, de Physique des Matériaux, et de Cosmochimie (IMPMC), UMR CNRS 7590, Sorbonne Universités, Muséum National d'Histoire Naturelle, CP 52, 57 rue Cuvier, Paris F-75231, France.

[5]Instituto de Geociências, Universidade de São Paulo, Rua do Lago 562, Cidade Universitária, São Paulo, 05508-080, Brazil.

[6]Géosciences Montpellier, Université de Montpellier, CNRS, Université des Antilles, 34095, Montpellier, France.

Abstract

The Fe isotopic compositions of mantles of differentiated inner solar system bodies are similar to, or heavier than those of chondritic meteorites. Core–mantle differentiation is a potential contributor to planetary isotopic fractionation. However, previous metal–silicate experiments provide only equivocal evidence for such fractionation, and have been used to argue that the Ni content of core-forming metal influences the extent of Fe isotopic fractionation. Here, we complement existing data with twenty-two novel metal–silicate

equilibrium experiments with varying Ni content to better quantify the effect of Ni on the vector and magnitude of Fe isotopic fractionation during core formation. We find no statistically resolvable effect of the Ni content in the metallic phase on the metal–silicate Fe isotopic fractionation factor over a wide range of Ni concentrations (0 to 70 *wt.%* in the metal). In particular, the Fe isotopic composition of alloys from two experiments performed with 70 *wt.%* of Ni ($\delta^{56}Fe_{metal}$=0.27±0.04‰ and 0.32±0.03‰, 2 standard deviations σ) are identical to the bulk experimental starting material ($\delta^{56}Fe_{bulk}$=0.27±0.10‰, 2σ). Our data across all experiments yield an average isotopic fractionation factor $\Delta^{56}Fe_{met–sil}$=0.05±0.22‰ (2σ) at 1873 K and 1–2 GPa, suggesting that little to no isotopic fractionation of Fe is expected to occur during core formation at low pressures. As such, our data does not support core formation as the main mechanism causing the observed variability in Fe isotope ratios between the silicate Earth, Moon, Vesta and other differentiated asteroids. A combination of multiple accretion-related processes—including condensation from the solar nebula, volatile-depleting events such as giant impacts, and the disproportionation of ferrous iron to ferric iron and iron metal in larger bodies—as well as deep mantle and recycling processes could explain the heavier-than-chondritic signatures in the silicate Earth and Moon. Furthermore, our results support the ideality of mixing among Fe–Ni alloys, as previously demonstrated for physical properties but less conclusively evidenced for chemical properties.

Introduction

Experimental determination of isotopic fractionation of siderophile elements between metal and silicate has been used to investigate core formation on planetary bodies (*e.g.* Georg et al., 2007; Bourdon et al., 2018). Isotopic fractionation recorded in laboratory experiments can be compared to natural isotope signatures, providing a powerful tool for interpretation of isotopic variations among planetary materials and refining our knowledge of their history in

the early solar system. In principle, these experiments involve equilibration of molten silicate and molten metal at high pressure and high temperature until elemental and isotopic equilibrium between the two phases is reached. The silicate glass and metal grains from each quenched experiment are physically separated and their isotope compositions are determined. Such studies on various siderophile elements can be used to trace the conditions of planetary differentiation—its temperature (Hin et al., 2014), its pressure (Labidi et al., 2016), redox conditions (Dalou et al., 2019), subsequent rehomogenisation mechanisms (Kempl et al., 2013), and the composition of the core (Savage et al., 2015; Mahan et al., 2017; Xia et al., 2019). Applied to volatile elements, they open the possibility to trace the timing and origin of planetary volatile delivery (Kubik et al., 2021b). Such results allow the isotopic characterisation of the building blocks that eventually accreted to form planetary bodies (Hin et al., 2014), permitting assessment of whether core formation is the main planetary process controlling the abundances and isotopic compositions of certain elements in the accessible mantle of the body. Alternatively, other possible mechanisms such as magmatic differentiation (Bonnand et al., 2016) or volatilisation processes (Xia et al., 2019) may be required. Numerous key questions may thus be addressed through experimental evidence. However, experimentally-determined isotopic fractionation factors from different studies are often in disaccord with one another, namely, Zn (Bridgestock et al., 2014; Mahan et al., 2017; Xia et al., 2019), Si (Shahar et al., 2009,2011; Hin et al., 2014; Kempl et al., 2013), Ni (Lazar et al., 2012; Guignard et al., 2020), Cu (Savage et al., 2015; Xia et al., 2019). These discrepancies are partially attributable to differences in the experimental approach. In this respect, replication of such experiments combined with independent, analytical determination of the isotopic consequences of core formation (*e.g.* Georg et al., 2007; Moynier et al., 2011) can only be beneficial to the general understanding of planetary differentiation.

Planetary materials show significant variability in their Fe isotopic compositions. Ordinary, enstatite and carbonaceous chondrites have an average δ^{56}Fe (per mil variation of the $^{56}Fe/^{54}Fe$ ratio relative to IRMM-014) of 0.00±0.01‰ (2σ) (Craddock and Dauphas, 2011; Schoenberg and von Blanckenburg, 2006; Wang et al., 2013, 2014). The terrestrial mantle is estimated to have a δ^{56}Fe=0.03±0.02‰ (Craddock et al., 2013; Sossi et al., 2016a; Weyer and Ionov, 2007) while mid-ocean ridge basalts (MORB) are isotopically heavier with average δ^{56}Fe=0.10±0.01‰ (Teng et al., 2013; Craddock et al., 2013; Craddock and Dauphas, 2011; Nebel et al., 2018; Weyer and Ionov, 2007). Even after accounting for the effect of olivine crystallisation and correcting their Fe isotopic composition back to that of a primary melt in equilibrium with mantle peridotite, MORBs define an average δ^{56}Fe=0.07±0.01‰ (Sossi et al., 2016a; Nebel et al. 2018), heavier than chondritic meteorites. By contrast, primary melts of the martian and vestan mantles, determined respectively from the SNC (shergottite-nakhite-chassignite) and HED (howardite-eucrite-diogenite) groups of meteorites, have near-chondritic isotopic signatures (Poitrasson et al., 2004; Schoenberg and von Blackenburg, 2006; Wang et al., 2012; Sossi et al., 2016b) whereas angrites are markedly heavier (δ^{56}Fe=0.12±0.04‰, n=7, Wang et al., 2012). Lunar basalts yield a range of isotopic compositions from near-chondritic to 0.3‰ (Weyer et al., 2005; Poitrasson et al., 2004; Liu et al., 2010; Wang et al., 2015; Sossi and Moynier, 2017; Poitrasson et al., 2019), but ferroan anorthosites and Mg suite rocks from the lunar highlands define an estimated bulk lunar Fe isotope composition similar to that of the Earth's mantle (δ^{56}Fe=0.05±0.03‰, Sossi and Moynier, 2017; Poitrasson et al., 2019).

Several processes have been proposed to account for this Fe isotopic variability including (1) volatile loss by vaporisation during the Moon-forming giant impact (Poitrasson et al., 2004; Poitrasson 2007; Liu et al., 2010), (2) accretion from the solar nebula associated with various degrees of nebular or post-nebular Fe loss in planetary building blocks (Sossi et

al., 2016b), (3) disproportionation of ferrous iron (Fe^{2+}) into Fe^{3+} and metallic iron by bridgmanite crystallisation during accretion in bigger planetary bodies such as the Earth (Williams et al., 2012; Frost and McCammon, 2008), (4) core–mantle equilibration related isotopic fractionation at either high (Polyakov, 2009) or low pressures (Elardo and Shahar, 2017) and (5) deep mantle recycling processes (Smith et al., 2021; Soderman et al., 2021). Lesher et al. (2020) argued that the upper part of the Earth's core could be enriched in heavier Fe isotopes by thermo-diffusion over time. If this isotopically heavier Fe is, as suggested in the study, transported to the upper mantle by ascending plumes, it could explain the heavy Fe isotopic signature of the BSE (bulk silicate Earth). However, core–mantle equilibration remains the largest chemical mass transfer process that occurred on Earth, suggesting that it may have a significant contribution in defining the observed isotopic signatures of its present-day core and mantle. It is therefore paramount to understand the isotopic behaviour of Fe during core–mantle equilibration.

However, the degree and direction of Fe isotope fractionation between silicate and core-forming alloy is influenced by a variety of parameters. Early experimental work addressing this question did not find any resolvable Fe isotopic fractionation between S-free metallic and silicate phases over a range of pressures, from 1 to 60 GPa (Poitrasson et al., 2009; Hin et al., 2012; Shahar et al., 2015; Liu et al., 2017), leading to the conclusion that, at the high temperatures required for core formation on terrestrial bodies (≥ 2000 K, *e.g.,* Righter and Drake, 1996), equilibrium isotope fractionation between metal and silicate—which is proportional to $1/T^2$—should be negligible compared to the observed variations. Liu et al. (2017) reported evidence up to 60 GPa of the insensitivity of Fe force constant to pressure in both metal and silicate materials, which supports the relevance of low-pressure studies using the piston cylinder and isotopic measurements on the synthesised phases to address Fe isotopic fractionation during core formation. Although some of the

metallic phases investigated contained a small fraction of Ni (~5–9 *wt.%*) as is relevant to planetary cores (5 *wt.%* in the Earth's core; Palme and O'Neill, 2014), the effect of Ni on iron isotope fractionation was not explicitly investigated prior to the study of Elardo and Shahar (2017). They reported piston cylinder experiments conducted at 2123 K and 1 GPa in which the Ni content of the metal varied between 1 and 26 *at.%*, and observed a systematic increase of the Fe isotopic fractionation factor with Ni content, which defines the following relation: $\Delta^{57}Fe_{met\text{-}sil}$=0.011(Ni, *at.%*)+0.04‰. Thus, adding Ni to the metal phase enhances the Fe isotopic fractionation between metal and silicate, leading to an enrichment of the silicate in the lighter Fe isotopes relative to the metal. This result differs from that obtained with nuclear resonant inelastic X-ray scattering spectroscopy (NRIXS) results by Liu et al. (2017) suggesting that the force constant of iron bonds in Fe alloys is unaffected by the addition of Ni (up to 8 *wt.%*). Because the sense of this isotopic fractionation is opposite to that observed in the mantles of differentiated bodies, Elardo and Shahar, (2017) invoked significant isotopic fractionation during partial melting to restore the light subchondritic mantle isotopic composition inferred from their experiments to the superchondritic values observed in basaltic achondrites (*e.g.* Sossi et al. 2016a). Importantly, such an isotopic effect implies that Fe–Ni alloys may not mix ideally, where ideal mixing is expected to induce no change in physical and chemical properties with varying Ni contents in the alloy. Therefore, a dependence of Fe isotopic fractionation on the Ni content is at odds with the constancy of density, compressibility, and wave velocities of Fe–Ni alloys with increasing Ni content (*e.g.* Lin et al., 2003; Kantor et al., 2007; Martorell et al., 2013; Badro et al., 2014). In other words, the properties of Fe–Ni alloys provide no evidence that the bonding environment of Fe in Fe–Ni alloys is modified by varying the proportion of Ni that would otherwise be necessary to generate an isotopic fractionation. Moreover, Fe–Ni ideality has been assumed in numerous experimental studies on core formation processes in which the effect of Ni was neglected. Xia

et al. (2019) reported Zn and Cu metal–silicate isotope fractionation experiments with significant sensitivity to the Ni content of the metal. However, the positive Ni-induced isotopic fractionations were measured for Fe (Elardo and Shahar, 2017), Zn and Cu (Xia et al., 2019), were based on fewer than 10 experiments for each element. More experimental results, involving a broader range of Ni contents, are needed to establish whether there is a resolvable effect of the Ni content of an Fe–Ni alloy on various chemical and isotopic parameters. Therefore, assessing the Fe isotopic fractionation between metal and silicate has profound implications for our understanding of core formation processes and for the physical and chemical properties of core-forming alloys.

To address this question, twenty-two novel metal–silicate equilibrium experiments were performed in order to characterise the effect of Ni on the Fe isotope fractionation. In particular, a wider range of Ni content in the metal (from 0 to 70 *wt.%*) was covered compared to previous studies (0 to 25 *wt.%*, Elardo and Shahar, 2017).

Method

Experimental method

Mixtures composed of 70 *wt.%* of a crushed mid-ocean ridge basalt (MORB) (Kubik et al., 2021a) with varying proportions of pure Fe and Ni were prepared by weighing each component and grinding them in an agate mortar until complete homogenisation was achieved. All experiments were performed in a 150-ton end-loaded piston cylinder apparatus at the Institut de Physique du Globe de Paris (IPGP, Université de Paris), in ½" talc pyrex assemblies using graphite furnaces. Pressure calibration of the apparatus was performed using the alumina concentration in orthopyroxene in equilibrium with pyrope in a $MgO–Al_2O_3–SiO_2$ system (Perkins and Newton, 1981). The friction coefficients reported by McDade et al. (2002) were compared and found to be identical to the coefficients measured during the

calibration of the apparatus, allowing similar corrections to be applied for friction loss for assembly materials. During the experiments, the temperature was measured using a type D ($W_{97}Re_3/W_{75}Re_{25}$) thermocouple contained in a 4-hole alumina sleeve just above the capsule lid. Uncertainties on pressure and temperature are estimated to be around 0.1 GPa and 50 K (Siebert et al. 2011). All experiments were performed at 1 to 2 GPa and at 1873 K in order to induce complete fusion and promote equilibrium between metal and silicate in the system. Four capsule types—boron nitride, crushable MgO, single-crystal MgO and graphite—were tested in order to assess their effect on the Fe isotopic fractionation factor.

Sample collection and purification

The metal and silicate phases were separated mechanically after each experiment. Clean pieces of each phase were selected carefully under magnifying glass. Metal pieces were directly dissolved in 6 N HCl. Silicate samples were sorted in order to select clean pieces devoid of metal beads or capsule material. These pieces were roughly crushed and a magnet was used to remove any stray pieces of metal (Kubik et al., 2021b). The silicate was finely crushed in an agate mortar and digested in a 1:3 solution of HF:HNO_3 in closed Teflon bombs on a hotplate at 100°C. Silicate samples were then dried and further digested in aqua regia on a hot plate at 150°C to remove any residual fluoride complex. They were dried again and dissolved in 6 N HCl for purification. The purification of Fe in the samples was performed following the method described in Sossi et al. (2015), by anion exchange chromatography using AG1-X8 (200-400 mesh) and 0.4 × 7 cm custom-made Teflon columns. Columns were filled with 1 mL AG1-X8 resin and cleaned with 5 mL 3 N HNO_3, 5 mL H_2O and conditioned with 5 mL 6 N HCl. The samples were subsequently loaded in 0.5 mL of 6 N HCl. The matrix was eluted with 11 mL of 6 N HCl. The Fe cuts were eluted with 3 mL of 0.5 N HCl, and dried to be redissolved in 0.5 N HNO_3. They were diluted to 4 ppm Fe solutions and spiked

196 with 8 ppm of Ni, following the method described in Sossi et al. (2015). This protocol yielded
197 procedural blanks inferior to 10 ng (n=2) (Kubik et al., 2021c).

198 ## MC-ICPMS measurements

199 Iron isotopic measurements were performed on a Neptune Plus MC-ICPMS at IPGP
200 (Université de Paris), used in medium resolution mode. The cups were configured as
201 described in Sossi et al. (2015) in order to collect the intensity on the masses 53, 54, 56, 57,
202 60 and 61. The mass 53 was used to correct for any ^{54}Cr interference on ^{54}Fe, even though
203 chromatographic separation was shown to be very efficient, meaning the correction was
204 insignificant (^{53}Cr signals were ~5×10^{-5} V, indistinguishable from 2% HNO_3 blanks). The
205 ^{61}Ni/^{60}Ni ratios measured in all samples were used to correct for mass bias effects.
206 Measurements of IRMM-014 performed in between samples were used to calculate the delta
207 values reported in this study. International reference materials were measured along with the
208 experimental samples with Fe isotopic compositions reproducing the previously published
209 values (*e.g.* for BHVO-2: δ^{56}Fe=0.10±0.04‰, 2σ).

210 ## Evidence of metal–silicate equilibrium

211 Two methods are typically used to assess metal–silicate isotopic equilibrium in high-
212 temperature experiments: time series and the "three-isotope method". Elemental equilibrium
213 can be reached very quickly at superliquidus conditions in metal–silicate experiments (5
214 seconds at 2300 K, Thibault and Walter, 1995). As diffusion rates for elemental exchange
215 cannot necessarily be extrapolated to those for isotopic exchange rate, several experimental
216 studies report that isotopic exchange can be both faster than chemical diffusion (Lesher et al.,
217 1990; Van der Laan, 1994) and slower (*e.g.* Guignard et al., 2020; Shahar et al., 2008). In this
218 context, numerous studies report relatively short equilibration time experiments (*e.g.* Hin et
219 al., 2013; Kubik et al., 2021b; Poitrasson et al., 2009; Shahar et al., 2011). The attainment of
220 isotopic equilibrium after a few minutes can be explained by the superliquidus temperatures

reached, at which the entire sample is molten. The molten state promotes equilibration because (1) diffusion rates are significantly higher in liquids state than in a solid phase, (2) convection further stirs the melt inside the capsule, owing to the small thermal gradient endemic to high pressure experiments, (3) homogenisation is additionally favoured by using a finely crushed powder as a starting material. Time series experiments are an empirical way to establish the time needed to achieve equilibrium. In this study specifically, (a) thorough SEM and EDX characterisation of each phase provided proof that the entirety of the sample material was fully molten and resulted in (b) chemically homogeneous phases (see Figures S1, S2, S3 and supplementary information) as well as (c) textural equilibrium evidenced by one large spherical metal blob (Néri et al., 2021). (d) The Fe isotopic fractionation factors follow a systematic trend that can be statistically determined to good precision due to an extensive data set comprising 22 experiments. (e) Repeated time series experiments show no statistically resolvable evolution of the Fe isotopic fractionation factor between runs of 3- and 30-minute duration (see supplementary information and Figure S4). Experiments with durations of 30 minutes or more exhibiting greater variability, with both positive and negative isotopic fractionation factors observed. This enhanced variability in longer experiments is attributed to progressive reaction of the silicate melt with the capsule material over time. Moreover, the isotopic results reported in this study are in agreement with several other studies performed in a range of laboratory facilities with different methodologies and apparatuses (Poitrasson et al., 2009; Hin et al., 2012; Liu et al., 2017; Elardo and Shahar, 2017, Figure 1a). The results from our study are also in agreement with numerous pieces of evidence of Fe–Ni alloy ideality (Lin et al., 2003; Kantor et al., 2007; Martorell et al., 2013; Badro et al., 2014; Huang and Badro, 2018). With respect to demonstration of isotopic equilibrium, the three-isotope method was not included in the protocol of this study. Although Cao and Bao (2017) and Bourdon et al. (2018) reported artifacts that could induce non-linear

246 trajectories, leading the authors to delineate limitations of the method, other studies have
247 argued for its robustness (Shahar et al., 2008; Shahar and Young, 2020), and in particular its
248 usefulness in verifying that the system remained closed with respect to mass exchange
249 throughout an experiment. In this study, the use of single-crystal MgO capsules was
250 employed to ensure minimal chemical and isotopic interaction with the capsule (see
251 supplementary information). Moreover, the "lever rule method", consisting in the
252 recalculation of the bulk isotope composition of the experiments based on measured $\delta^{56}Fe$ of
253 each phase by mass balance yields a good reproducibility (on average $\delta^{56}Fe_{final\ bulk}$=0.40±0.08‰, 1σ). The three-isotope method is predicated on experiments that preserve a
255 record of the approach to equilibrium between two phases, and thus represent a form of time-
256 series in which equilibration times are necessarily slow. Because equilibrium is achieved
257 within a few minutes in our experiments, the three-isotope method is unfeasible from an
258 experimental standpoint. Namely, the timescale of equilibration of the piston cylinder
259 assembly to ensure stable conditions (*e.g.*, Matjuschkin et al., 2015) is of the same order of
260 that required for the three-isotope method to produce dispersion in isotope composition. Each
261 bulk starting material used in this study was also measured for Fe isotopes and are found to
262 reproduce the calculated bulk value within error for 12 of them which further supports closed
263 system and achievement of equilibrium.

264 Iron isotopic behaviour in metal–silicate equilibrium experiments

265 Twenty-two metal–silicate equilibrium experiments were performed at 1 and 2 GPa
266 and 1873 K. Run durations were varied between 3 and 60 minutes in order to assess the
267 timescales required to approach isotopic equilibrium. Petrographic observations indicate that
268 the starting material was fully molten in all experiments (see Figure S1). The metal coalesced
269 into a discrete sphere in most experiments, and subsequent to quenching, was separated

mechanically from the silicate phase. All experimental parameters and isotopic measurements are available in Table 1.

Iron isotope fractionation results for all experiments from this study and literature are presented in Figure 1a. It should be noted that experiments from other studies were carried out at different temperatures and were therefore recalculated at 1873 K for comparison with the dataset reported herein by using the relationship $\Delta^{56}Fe_{metal-silicate} = a \cdot \frac{1}{T^2}$ (*e.g.* Urey, 1947). Our results show no correlation between the Ni content of the metal and the Fe isotopic fractionation factor between metal and silicate (Figure 1b). There is also no resolvable difference in isotopic fractionation factor between the experiments using the different types of capsules (boron nitride, crushable MgO, single-crystal MgO and graphite), although from petrographic observations, use of the single-crystal MgO capsules minimises the extent of reaction between capsule and sample by containing the interactions within the first 30 µm of the capsule. Isotope measurements on multiple parts of experiment E375 are presented in Figure 2. This short-duration experiment exhibits a glassy silicate in the center and partially crystallised silicate towards the capsule boundary where skeletal olivine crystals grew as a result of MgO enrichment and the relatively low quenching rates achievable in the piston cylinder (*e.g.* Green et al., 1975). Measurements on these separated parts show no difference in Fe isotopic composition between glass and crystalline silicates (δ^{56}Fe=0.30±0.08‰ and 0.29±0.11‰ respectively, 2σ) which means that MgO diffusion towards the center of the sample does not affect the Fe isotope composition of the silicate. Therefore, in this particular case, MgO capsules are well-suited for isotope fractionation experiments with respect to MgO diffusion. In this experiment, the isotopic composition of the metal is identical to that of the silicate. The first 30 µm of the capsule in contact with the melt containing less than 4 *wt.%* of Fe, however, exhibits a clear enrichment in light Fe isotopes, even after a few minutes (δ^{56}Fe=-0.72±0.02‰, 2σ). However, we estimate that this

295 Fe-bearing rim in the capsule contains less than 1.5% of the total Fe budget introduced in the
296 capsule. In this context, light Fe contained in the rim, which represents less than 3% of the
297 inner capsule volume, creates a shift of the bulk sample Fe isotopic composition of 5.5%
298 relative at most, which is within the analytical uncertainty and therefore not resolvable by our
299 measurements. At such superliquidus temperatures, chemical reactions between the capsule
300 and the sample progress with increasing run duration. Therefore, in the long term, measured
301 isotopic fractionations could be driven by interactions between the capsule and the sample,
302 even if no correlation is observed between the isotopic fractionation and the time duration in
303 the reported data set (see Figure S4). However, in this experiment, even with a limited
304 reservoir of Fe on the boundaries of the sample that results in light isotopic composition
305 created by Fe loss, the final bulk isotopic composition of the experiment calculated by mass
306 balance of the silicate and metal compositions (0.29±0.06‰, 2σ) is identical to the isotopic
307 composition of the starting material (0.30±0.08‰, 2σ). This suggests that the limited Fe loss
308 resulted in insignificant and unresolvable isotopic fractionation of the experimental sample.
309 The detection of Fe only in the first 30 µm of the capsule in all single-crystal MgO
310 encapsulated experiments suggest that such capsules permit near-closed system conditions in
311 the experimental sample.

312 Iron isotopic fractionation factors from this study yield an average of $\Delta^{56}Fe_{met-}$
313 $_{sil}$=0.05±0.22‰ (2σ). This means that these results are not significantly different from 0.0‰,
314 and no dependence on the Ni content of the metal is detected over a wide range of Ni
315 concentrations. The scatter of the data set, although noticeable, is of the same order of
316 magnitude or lower than previous studies using the same method (see Supplementary
317 Information and Table S1).

318 **Figure 1: Results of Fe isotopic fractionation in metal–silicate equilibrium experiments.** Error bars correspond to 2
319 standard deviations (2σ) propagated from the errors on metal and silicate Fe isotopic measurements. **a.** $\Delta^{56}Fe_{metal–silicate}$ of all
320 experiments of this study and from literature recalculated at 1873 K (Poitrasson et al., 2009; Hin et al., 2012; Elardo and
321 Shahar, 2017) as a function of the Ni content of the metallic phase. The horizontal dashed line with orange error represents
322 the average fractionation factor of all experiments presented on the graph, *i.e.* 0.04±0.09‰ (1σ). The dotted line represents

the trend of Ni content dependency on Fe isotopic fractionation factor determined by Elardo and Shahar (2017). **b.** $\Delta^{56}Fe_{metal-silicate}$ for all experiments of this study. Squares are experiments carried out in graphite capsules, circles correspond to the ones in crushable MgO capsules, triangles for experiments using boron nitride capsules and diamonds for experiments carried out in single-crystal MgO capsules. Experiments are color coded according to their time durations: white for 1-5 minutes, pale green for 15 minutes, light green for 30 minutes, and dark green for 60 minutes. The horizontal dashed line with grey error represents the average of all experiments presented on graph a., *i.e.* 0.04±0.09‰ (1σ).

Figure 2: Results of Fe isotopic compositions on a single experiment. E375 was performed at 2 GPa and 1873 K in a single-crystal MgO capsule with a time duration of 5 minutes. Its metal phase contains 5 *wt.%* of Ni. The displayed errors correspond to 2σ on the measurements. Iron isotopic measurements were performed on two silicate samples—a central glassy part and an outlying crystallised part—as well as the metal phase and the capsule. The two silicate parts and the metal present identical isotopic composition to the starting material whereas the inner part of the capsule (inner 30 µm) is enriched in light Fe isotopes. The diffusion of MgO from the capsule has no effect on the Fe isotopic composition of the silicate phase and the Fe loss as detected by a light isotopic composition in the capsule is not sufficient to induce a resolvable fractionation of the sample towards heavier Fe isotopic compositions.

The Fe isotopic compositions of the bulk starting materials were measured to assess potential Fe loss during the experiments (Table 1). These measured Fe isotope compositions of the starting material (initial bulk) were compared to bulk values calculated by mass balance from the Fe isotopic composition of the metal and silicate from the run products (final bulk, Figure 3). Although there is no clear correlation between the fractionation factor and the agreement between the initial and final bulk values (see also Figure S5), both estimations of the bulk experimental Fe isotope composition coincide within error for 12 out of the 22 experiments of the reported data set. This indicates that experiments largely approached closed system behaviour, resulting in limited loss of Fe through the capsule. Thorough characterisation of the Fe content of experimental capsules after the experiments showing moderate Fe diffusion into the capsules also corroborates closed system behaviour, a necessary condition to properly investigate isotope fractionation processes experimentally. Iron loss quantified by the difference between the measured and calculated bulks shows that single-crystal MgO and graphite capsules present reduced Fe loss with respect to other capsule types (Supplementary Figure S5).

Figure 3: Comparison of initial and final Fe isotope compositions of bulk experiments. The thick blue line and associated error represents the average Fe isotope composition measured from the powder mixtures used as starting materials in the experiments and 2σ on the measurements. Because the MORB contains c.a. 6 *wt.%* Fe with a different Fe isotopic composition from the Fe dopant, the starting material presents an intermediate Fe isotopic composition between that of the two Fe-bearing components, namely the MORB (light blue line) and the Fe dopant (dark blue line). The symbols correspond to calculated Fe isotope compositions of final bulk experiments from mass balance using metal and silicate Fe isotopic measurements for each experiment (equation given on the figure). The error bar of each symbols corresponds to 2σ propagated from uncertainties on the Fe isotopic and Fe elemental measurements. The symbol shapes correspond to different capsule types. Symbols presenting a horizontal-line pattern correspond to experiments producing a metal–silicate fractionation factor superior to 0.06‰. Final bulk value symbols are color-coded according to the run duration: white for 1–5 min, pale green for 15 min, light green for 30 min and dark green for 60 min.

Fig. 4 displays the Fe isotope composition of single experimental phases from this study and Elardo and Shahar (2017) as a function of metal Ni content. The Ni-induced Fe isotope fractionation proposed by Elardo and Shahar (2017) implies that such a fractionation is driven by the composition of the metallic phase as Ni is almost exclusively hosted in the metallic phase. Therefore, a clear variation of the metal Fe isotope composition should be observed as a function of the metal Ni content. However, no systematic change in the metal Fe isotope composition is reported in the data set from this study (Figure 4a). In fact, the composition of both experiments performed with 70 *wt.%* of Ni ($\delta^{56}Fe_{metal}$=0.27±0.04‰ and 0.32±0.03‰, 2σ) are strictly identical to the measured bulk experimental starting material (0.27±0.10‰, 2σ). It should be noted that these two experiments also underwent negligible Fe loss (Figure 3). This constitutes strong evidence for a very limited effect of Ni on the Fe isotopic fractionation at the experimental conditions of this study. The silicate Fe isotopic compositions present a more scattered distribution (Figure 4b), likely due to moderate interactions with the capsule, and equally show no correlation with the metal Ni content. Experiments contained in crushable MgO and BN have on average heavier Fe isotopic signatures in both the metal and the silicate, compared to single-crystal MgO and graphite capsules. This is likely due to higher Fe loss permitted by faster diffusion in these materials. However, we show that Fe loss is limited in all of our experiments (Figure 3) and importantly does not correlate with the Fe isotopic fractionation results (Figure S5). Therefore, the limited Fe loss occurring during the experiments presented in this study is either i) not significant enough and/or ii) occurs over a timescale slower than for metal–silicate equilibrium. As a result, the degree of Fe loss appears not to affect the Fe isotopic fractionation factor. Iron isotope compositions of single experimental phases from Elardo and Shahar (2017) show a clear correlation with Ni content (Figures 4c and d). However, this is due to the fact that the silicate fraction of the starting mixtures was spiked with ^{54}Fe, resulting in starting materials

with variable Fe isotope compositions with respect to their Ni content (Figures 4c and d). The observed trends therefore reflect differences in the starting material rather than a metal–silicate isotope fractionation. We speculate that if this effect could be corrected by recalculating all the experiments for the same bulk starting material composition (by using the precise proportions of each component and/or Fe isotope compositions of starting materials as reported in our study), an effect of Ni content on the Fe isotope composition may not be detectable. Considering comprehensive literature data and the novel experimental metal–silicate data set reported in this study, we conclude that there is no evidence for Ni-induced Fe isotope fractionation between metal and silicate.

Figure 4: Iron isotopic composition of separate phases from experiments reported in this study and Elardo and Shahar (2017) as a function of the metal Ni content. Error bars represent 2σ on the isotopic measurements. **a.** Iron isotope composition of metal phases from this study. **b.** Iron isotope composition of silicate phases from this study. **c.** Iron isotope composition of metal phases from Elardo and Shahar (2017). **d.** Iron isotope composition of silicate phases from Elardo and Shahar (2017).

Table 1: Iron isotopic compositions of run products and parameters for all experiments of this study performed at 1873 K, as well as compositions of all starting materials. Replicated samples were split before column separation. The reported errors correspond to 2 standard deviations.

Run	P (GPa)	Ni (*wt.%*)	Time (min)	Capsule	n	$\delta^{56}Fe_{metal}$	2σ	$\delta^{57}Fe_{metal}$	2σ	n	$\delta^{56}Fe_{silicate}$	2σ	$\delta^{57}Fe_{silicate}$	2σ	$\Delta^{56}Fe_{met-sil}$	2σ	$\Delta^{57}Fe_{met-sil}$	2σ
E269	1	20	15	MgO	4	0.48	0.02	0.73	0.03	4	0.40	0.04	0.61	0.05	0.08	0.04	0.12	0.06
E270	1	10	15	MgO	5	0.51	0.05	0.78	0.08	5	0.50	0.03	0.75	0.03	0.01	0.03	0.02	0.03
E271	1	20	60	MgO	4	0.51	0.03	0.77	0.06	4	0.39	0.01	0.60	0.05	0.12	0.03	0.17	0.05
E276	1	30	15	MgO	3	0.49	0.10	0.73	0.12	3	0.30	0.04	0.46	0.04	0.19	0.06	0.27	0.06
E298	2	30	15	MgO	3	0.49	0.03	0.75	0.04	3	0.49	0.01	0.78	0.03	0.00	0.02	-0.02	0.03
E302	2	0	15	MgO	3	0.49	0.08	0.75	0.10	3	0.47	0.04	0.72	0.04	0.02	0.06	0.04	0.04
E318	2	30	15	SC MgO	4	0.48	0.09	0.68	0.10	4	0.47	0.06	0.65	0.10	0.00	0.11	0.03	0.14
E320	2	0	3	BN	4	0.48	0.06	0.71	0.05	4	0.33	0.11	0.50	0.18	0.15	0.13	0.21	0.19
E321	2	30	15	BN	3	0.42	0.16	0.64	0.04	3	0.36	0.04	0.57	0.15	0.05	0.07	0.07	0.15
E322	2	30	15	MgO	3	0.49	0.10	0.70	0.16	3	0.36	0.04	0.52	0.05	0.13	0.06	0.17	0.08
E323	2	0	3	BN	2	0.51	0.01	0.77	0.01	2	–	–	0.54	0.15	–	–	0.23	0.15
E324	2	30	3	MgO	2	0.55	0.21	0.78	0.31	2	0.38	0.06	0.58	0.08	0.17	0.22	0.20	0.32
E325	2	70	3	MgO	2	0.32	0.03	0.47	0.04	2	0.41	0.03	0.59	0.02	-0.09	0.04	-0.12	0.02
E373	2	30	15	SC MgO	4	0.32	0.08	0.44	0.17	4	0.28	0.04	0.43	0.02	0.04	0.09	0.01	0.17
E375 glass	2	30	5	SC MgO	4	0.29	0.06	0.41	0.08	4	0.30	0.09	0.40	0.15	-0.01	0.11	-0.02	0.16
E375 crystals										4	0.29	0.11	0.46	0.10				
E375 capsule										4	-0.72	0.02	-1.07	0.14				
E376	2	30	30	SC MgO	4	0.35	0.04	0.48	0.00	4	0.26	0.05	0.43	0.05	0.09	0.06	0.05	0.05
E377	2	70	30	SC MgO	4	0.26	0.05	0.40	0.06	4	0.21	0.08	0.25	0.08	0.06	0.08	0.14	0.12
E377 replicate					4	0.27	0.03	0.39	0.16									

E378	2	0	30	SC MgO	4	0.37	0.03	0.50	0.02	4	0.28	0.07	0.37	0.10	0.10	0.07	0.15	0.10
E378 replicate										4	0.25	0.04	0.34	0.11				
E379	2	10	30	SC MgO	4	0.38	0.05	0.55	0.08	4	0.15	0.04	0.21	0.11	0.23	0.06	0.35	0.13
E380	2	20	30	SC MgO	4	0.34	0.09	0.50	0.16	4	0.51	0.09	0.73	0.16	-0.17	0.12	-0.23	0.23
E381	2	30	30	graphite	4	0.30	0.05	0.41	0.01	4	0.26	0.05	0.38	0.04	0.04	0.07	0.03	0.04
E382	2	30	60	SC MgO	4	0.30	0.09	0.44	0.12	4	0.54	0.05	0.81	0.01	-0.24	0.11	-0.37	0.12

Material	n	δ^{56}Fe	2σ	δ^{57}Fe	2σ
Fe dopant	5	0.47	0.08	0.69	0.06
MORB	5	0.09	0.05	0.11	0.08
Fe–Ni_0	4	0.33	0.10	0.47	0.24
Fe–Ni_{10}	4	0.28	0.04	0.45	0.14
Fe–Ni_{20}	4	0.26	0.03	0.38	0.17
Fe–Ni_{30}	4	0.30	0.08	0.45	0.23
Fe–Ni_{70}	4	0.27	0.10	0.42	0.20

Iron isotopic fractionation during core formation

Our experimental results include novel metal–silicate equilibrium Fe isotope fractionation data over a wide range of Ni content. There is presently no evidence that pressures above 2 GPa could generate an Fe isotopic fractionation between metal and silicate (Liu et al., 2017; Poitrasson et al., 2009). This allows us to interpret our experimental data in a context of core formation on large bodies such as the Earth, but also on smaller bodies such as Vesta without the need for pressure extrapolation. The large number of experiments in this study provides enhanced statistical accuracy and shows that Ni proportion in the metal has a limited effect on the Fe isotope fractionation between metal and silicate. While our conclusions may differ, the results presented here yield a similar range of Fe isotopic fractionation factors (Figure 1a) to those reported in the study of Elardo and Shahar (2017) (average and 1σ of 0.05±0.11 and 0.04±0.10 respectively) where the observed trend in Elardo and Shahar (2017) can be attributed to a relatively smaller number of experiments. In fact, the data presented herein, combined with that of Elardo and Shahar (2017) yields an average fractionation factor of $\Delta^{56}Fe_{met\text{-}sil}$=0.04±0.11‰ (1σ), indicating no isotopic fractionation

421 within uncertainty. Our results are also in agreement with previous experimental studies on Fe
422 isotopic fractionation (Poitrasson et al., 2009; Hin et al., 2012; Liu et al., 2017) demonstrating
423 the absence of Fe isotope fractionation at metal–silicate equilibrium as well as the absence of
424 a resolvable fractionation with addition of limited amounts of Ni (Poitrasson et al., 2009; Liu
425 et al., 2017). Significant S contents in the alloy may induce a positive metal–silicate isotope
426 fractionation with light isotope enrichment in the silicate (Shahar et al., 2014; Liu et al., 2017;
427 Pinilla et al., 2021). A similar trend of isotopic fractionation has been observed for other light
428 elements such as Si and C (Elardo et al., 2019; Shahar and Young, 2020). Nevertheless, this
429 vector of Fe isotopic fractionation is opposite to that observed in Earth's mantle and in the
430 mantles of other differentiated bodies relative to chondrites. Moreover, iron meteorites
431 present Fe isotopic signatures heavier than chondrites by 0.1–0.2‰ (δ^{57}Fe) (*e.g.* Williams et
432 al., 2006), such that heavy signatures in planetary mantles are unlikely to be established solely
433 by differentiation of chondritic material. Instead, the heavy signatures observed in iron
434 meteorites have been explained by core crystallisation with significant Fe isotopic
435 fractionation measured experimentally between solid and liquid iron alloys (Ni et al., 2020;
436 Young 2021). As such, to a first order there is no direct evidence that core–mantle segregation
437 causes significant isotopic fractionation of Fe, and hence is unlikely to control the isotopic
438 compositions of planetary mantles. Indeed, equilibrium isotope fractionation depends on $1/T^2$
439 so that enhanced fractionation is expected from low temperature core formation. However,
440 chondritic Fe isotopic values are observed in small bodies that underwent lower temperature
441 core formation such as Mars and Vesta (~1900 K, Righter and Drake, 1996) compared to the
442 non-chondritic Earth whose core equilibrated with the mantle at 2500–3500 K (Wood et al.,
443 2006). Therefore, core formation alone cannot explain the diversity of Fe isotope
444 compositions in the inner solar system. Other processes including various accretion and deep

mantle mechanisms need to be further investigated as potential causes for the Fe isotopic variability between inner solar system planetary bodies.

An increasing body of stable isotopic measurements on lunar rocks suggests that the Earth and the Moon share a common Fe isotope signature (Wang et al., 2015; Sossi and Moynier, 2017; Poitrasson et al., 2019), and isotopic differences are only observed among volatile elements that were depleted from the Moon. This result is in agreement with the widely-held view that volatilisation during Moon formation and evolution resulted in isotopic fractionation of multiple isotopic systems in the lunar mantle on a much larger scale than in Earth's mantle (*e.g.* Gargano et al., 2020; Kato et al., 2015; Pringle and Moynier, 2017; Sharp et al., 2010; Sossi et al., 2018a,b; Wang and Jacobsen, 2016; Wang et al., 2019; Wimpenny et al., 2022). The observation of isotopically heavy Fe isotope signatures in ureilites and angrites suggests that collisions between accreting bodies in the inner solar system may be common and that the observed signatures in inner planetary bodies are the result of contrasted accretional histories possibly involving multiple complex volatile-depleting events (Sossi et al., 2016b). The corollary states that Mars and Vesta suffered very limited syn- and post-accretion Fe loss as inferred from their chondritic signatures. The crystallisation of bridgmanite in large planetary bodies such as the Earth may enrich the mantle in heavy Fe isotopes (Williams et al., 2012) by disproportionation of Fe^{2+} into Fe^{3+} and metallic iron. Because metallic iron is isotopically lighter than ferric iron-bearing bridgmanite, its sequestration into Earth's core could produce a heavy Fe signature in the mantle without invoking volatilisation processes. Note however that such effects have not been confirmed so far by *in situ* NRIXS measurements and modelling of lower mantle crystallisation (Yang et al., 2019). Furthermore, this process would not explain the heavy isotope compositions of achondritic meteorites, notably the angrites, whose parent bodies were too small to have stabilised bridgmanite or Fe^{3+}-rich silicate melt (Armstrong et al., 2019) in equilibrium with

iron metal. Therefore, taken together, the aforementioned mechanisms provide possible means to explain the diverse Fe isotope signatures observed amongst inner solar system bodies.

Lesher et al. (2020) argued that the core–mantle boundary could be enriched in the heavier Fe isotopes and that pockets of isotopically heavy core-derived material could be entrained in plumes towards the upper mantle and crust. High temperature diffusion experiments over a thermal gradient of 250ºC could provide a mechanism for the enrichment of the outer core and lowermost mantle in heavy Fe isotopes. This process is predicted to be slower than the mantle convection and recycling according to the study. Therefore, the proposed mechanism to transport heavier Fe core diapirs in magmatic plumes towards the upper mantle could be tested by measurements on OIBs spanning a wide age range. Although a subsequent study on OIBs does not support the entrainment of core-derived liquids as the source of observed heavy OIB signatures (Soderman et al., 2021), the authors present a variety of potential processes explaining Fe isotopic variations in the mantle (*e.g.* subduction processes, hydrothermal alteration, contribution from sediments, peridotite and pyroxenite melting). Three main processes contributing to the establishment of heavy Fe isotope signatures in magmatic rocks are identified: (1) processes enriching eclogite in heavy Fe isotopes such as metamorphism, (2) lithospheric processing and (3) melting processes in conditions preventing the dilution of heavy Fe isotope-enriched melts with lighter isotope-enriched materials (Soderman et al., 2021). Diamond metallic inclusions with isotopically heavy signatures (Smith et al., 2021) that could not be explained by iron disproportionation were also proposed to have originated from deep recycling processes. Despite the propensity for these processes to generate isotopic variability locally, they are incapable of shifting the composition of the entire mantle over geological time. This conclusion is founded on the observation of the constancy in the Fe isotope compositions of komatiites through time

(Hibbert et al. 2012; Dauphas et al. 2010), and their concordance with those of peridotites that reflect the modern-day mantle (*e.g.* Weyer and Ionov, 2007).

On ideality in Fe–Ni alloys

The amount of Ni in the core is estimated to be around 5 *wt.%* based on geochemical and cosmochemical models (Palme and O'Neill, 2014). Numerous studies show that the physical properties such as density, compressibility, and wave velocities of Fe–Ni alloys vary only marginally as a function of their Ni content (e.g., Lin et al. 2003; Kantor et al. 2007; Asker et al., 2009; Martorell et al. 2013; Wakamatsu et al., 2018). Importantly, the constant density of such alloys does not uniquely constrain the amount of Ni in the core but implies that the entirety of the observed density deficit detected by seismological techniques (Birch, 1952) must be due to the presence of ~10% of light elements in the core (*e.g.* O, Si; Badro et al., 2015). Although the insensitivity of the physical properties of Fe–Ni alloys to the Ni content has been verified from multiple experimental studies (Lin et al., 2003; Kantor et al., 2007) and *ab initio* calculations (Martorell et al., 2013), this does not necessarily hold for their chemical properties.

Presently, studies investigating experimentally the elemental and isotopic behaviour of elements between metal and silicate that have considered the effect of the amount of Ni in the metal are very scarce, largely because it has been widely assumed to be negligible for the conditions relevant to core formation. Through the transpiration method and integration of the Gibbs-Duhem relation, early studies illustrated that the dissolution of Ni had little effect on the activity of Fe in binary alloys (Oriani, 1953; Zellars et al. 1959). As such, it is frequently assumed that the alloying of Fe with small quantities of Ni has a negligible effect on the behaviour of the metal. More recent Knudsen effusion mass spectrometric investigations of the activity–composition relations of liquid Fe–Ni alloys (Fraser and Rammensee, 1982) show that the activity coefficient of Fe, γFe, varies between 0.9 at X_{Ni}=0.5 to 1 at X_{Ni}=0.05 (with X

520 the mole fraction), with γFe remaining essentially ~1 up to X_{Ni} = 0.4 (Swartzendruber et al.
521 1991), exceeding the range for the metallic cores of rocky bodies. This therefore highlights
522 that for all likely core compositions, Fe dissolution in Fe–Ni alloys is ideal at ambient
523 pressures. Translation of Fe–Ni ideality to isotopic fractionation can be examined from a
524 crystal chemical standpoint. The activity coefficient is a manifestation of the energetics of
525 mixing between two compounds. That two phases (here, Ni (l) and Fe (l)) mix ideally implies
526 little to no energy penalty with respect to a mechanical mixture of these two phases. How
527 readily Ni substitutes into Fe depends upon the degree to which Ni distorts its structural and
528 electronic arrangement. Such a distortion can be described by the lattice strain model, and be
529 used to predict activity coefficients, where $\ln\gamma(Fe) = \Delta G_{Fe-Ni}^{strain}/RT$. Here, R is the gas
530 constant, T the absolute temperature and $\Delta G_{Fe-Ni}^{strain}$ the Gibbs free energy change of reaction
531 associated with the strain induced on the structure by the substitution (*e.g.* Wood et al. 2019).
532 Importantly, the quantity ΔGFe-Nistrain relates to the difference in bonding environment
533 (electronic charge & radius; *cf.* Blundy and Wood, 1994) between Fe and Ni, where a value of
534 0 leads to γ = 1 (*i.e.*, ideal behaviour). These same properties induce equilibrium stable
535 isotope fractionation (*e.g.*, Dauphas et al. 2014; Sossi and O'Neill, 2017). Waseda and Ohtani
536 (1974) measured the nearest-neighbour distances in pure liquid Fe and liquid Ni metals,
537 obtaining values very similar to one another at 1500 °C, 2.58 Å and 2.53 Å, respectively. That
538 γFe ~ 1 implies little distortion of the electronic and physical state of liquid Fe metal by the
539 substitution of up to ~40 mol % of Ni, meaning there is no driver for isotopic fractionation
540 associated with changing Ni content.

541 At higher pressures (up to 94 GPa), Huang and Badro (2018) demonstrated that Ni
542 (from 3.5 to 48.7 *wt.*% Ni) has no effect on the metal–silicate partitioning of Ni, Cr and V.
543 Our study suggests that the Ni fraction in an Fe–Ni alloy has no effect on Fe isotopic
544 behaviour in a metal–silicate equilibrium, also pointing towards chemical Fe–Ni ideality. Xia

et al. (2019) report contrasting observations, in which the magnitude of Zn and Cu isotope fractionation between metal and silicate was shown to be sensitive to the Ni content of the alloy, which could be due to specific interactions between Ni and these elements, owing to their disparate electronic arrangement and mean bond lengths. The 22 experiments reported herein not only enhance statistical accuracy but were also designed to explore a much broader range of Ni concentrations in the metal, from 0 to 70 *wt.%* (~25 *wt.%* maximum in Xia et al., 2020 and Elardo and Shahar, 2017). The assumption of chemical Fe–Ni ideality has extended implications regarding our understanding and knowledge of core formation related processes.

Conclusion

We performed 22 metal–silicate equilibrium experiments with the objective of establishing the effect of Ni content of Fe–Ni alloys on the Fe isotopic fractionation factor between metal and silicate. All experiments were carried out at 1–2 GPa and 1873 K, at which a variety of capsule materials were tested. An experimental time series, as well as petrographic analyses of the samples were performed in order to assess the conditions at which chemical equilibrium was achieved. No significant effect of Ni concentration on Fe isotope fractionation was detected over a wide range of Ni contents (0–70 *wt. %* in the metal fraction), supporting the common assumption of physical and chemical ideality of Fe–Ni alloys. Because the observed fractionation factor between metal and silicate is indistinguishable from zero, our data does not support core formation as the main mechanism causing the diversity in Fe isotope signatures observed amongst inner solar system planetary bodies. A combination of multiple accretion-related processes—including condensation from the solar nebula, volatile-depleting events such as giant impacts, and disproportionation of ferrous iron at high pressure in larger bodies—could together contribute to the observation of heavier-than-chondritic signatures in the Earth and the Moon's mantles.

Acknowledgement

We thank Stephan Borensztajn for technical support at the SEM platform. The authors thank Pascale Louvat for her support and indispensable expertise at the MC-ICPMS platform. The authors acknowledge the financial support of the UnivEarthS Labex program at Sorbonne Paris Cité (ANR-10-LABX-0023 and ANR-11-IDEX-0005-02). Part of the work was supported by IPGP multidisciplinary program PARI, by Région Île-de-France SESAME Grants no. 12015908, EX047016 and the IdEx Université de Paris grant, ANR-18-IDEX-0001 and the DIM ACAV+. JS acknowledges the financial support of the French National Research Agency (ANR Project VolTerre, grant no. ANR-14-CE33-0017-01). FM acknowledges funding from the European Research Council under the H2020 framework program/ERC grant agreement METAL.

Appendix A. Supplementary material

Research data and supplementary information to this article regarding isotopic equilibrium, time series and data variability can be found online at [doi].

References

K. Armstrong, D.J. Frost, C.A. McCammon, D.C. Rubie, T. Boffa Ballaran, 2019. Deep magma ocean formation set the oxidation state of Earth's mantle. Science 365, 903-906.

C. Asker, L. Vitos, I.A. Abrikosov, 2009. Elastic constants and anisotropy in FeNi alloys at high pressure from first-principle calculations. Phys. Rev. 79, 214112.

J. Badro, A. S. Cote, and J. P. Brodholt, 2014. A seismologically consistent compositional model of Earth's core. Proc. Natl. Acad. Sci., 111(21):7542–7545.

J. Badro, J.P. Brodholt, H. Piet, J. Siebert, F.J. Ryerson, 2015. Core formation and core composition from coupled geochemical and geophysical constraints. Proc. Natl. Acad. Sci., 112(40):12310–12314.

F. Birch, 1952. Elasticity and constitution of the Earth's interior. J. Geophys. Res., 57(2):227–286.

J. Blundy, B.J. Wood, 1994. Prediction of crystal–melt partition coefficients from elastic moduli. Nature, 372:452–454.

598 P. Bonnand, H. Williams, I. Parkinson, B. Wood, and A. Halliday, 2016. Stable chromium
599 isotopic composition of meteorites and metal–silicate experiments: Implications for
600 fractionation during core formation. Earth Planet. Sci. Lett., 435:14–21.

601 B. Bourdon, M. Roskosz, and R. C. Hin, 2018. Isotope tracers of core formation. Earth
602 Science Rev., 181(April):61–81.

603 L. J. Bridgestock, H. Williams, M. Rehkämper, F. Larner, M. D. Giscard, S. Hammond, B.
604 Coles, R. Andreasen, B. J. Wood, K. J. Theis, C. L. Smith, G. K. Benedix, and M.
605 Schönbächler, 2014. Unlocking the zinc isotope systematics of iron meteorites. Earth
606 Planet. Sci. Lett., 400:153–164.

607 X. Cao and H. Bao, 2017. Redefining the utility of the three-isotope method. Geochim.
608 Cosmochim. Acta, 212:16–32.

609 P. R. Craddock and N. Dauphas, 2011. Iron Isotopic Compositions of Geological Reference
610 Materials and Chondrites. Geostand. Geoanalytical Res., 35(1):101–123.

611 P. R. Craddock, J. M. Warren, and N. Dauphas, 2013. Abyssal peridotites reveal the near-
612 chondritic Fe isotopic composition of the Earth. Earth Planet. Sci. Lett., 365:63–76.

613 N. Dauphas, F.Z. Teng, N.T. Arndt, 2010. Magnesium and iron isotopes in 2.7 Ga Alexo
614 komatiites: Mantle signatures, no evidence for Soret diffusion, and identification of
615 diffusive transport in zoned olivine. Geochim. Cosmochim. Acta 74, 3274-3291.

616 N. Dauphas, M. Roskosz, E.E. Alp, D.R. Neuville, M.Y. Hu, C.K. Sio, F.L.H. Tissot, J. Zhao,
617 L. Tissandier, E. Médard, C. Cordier, 2014. Magma redox and structural controls on
618 iron isotope variations in Earth's mantle and crust. Earth Planet. Sci. Lett., 398:127–
619 140.

620 C. Dalou, E. Füri, C. Deligny, L. Piani, M. C. Caumon, M. Laumonier, J. Boulliung, and M.
621 Edén, 2019. Redox control on nitrogen isotope fractionation during planetary core
622 formation. Proc. Natl. Acad. Sci. U. S. A., 116(29):14485–14494.

623 S. M. Elardo and A. Shahar, 2017. Non-chondritic iron isotope ratios in planetary mantles as a
624 result of core formation. Nat. Geosci., 10(4):317–321.

625 S. M. Elardo, A. Shahar, T. D. Mock, and C. K. Sio, 2019. The effect of core composition on
626 iron isotope fractionation between planetary cores and mantles. Earth Planet. Sci.
627 Lett., 513:124–134.

628 D. G. Fraser and W. Rammensee, 1982. Activity measurements by Knudsen cell mass
629 spectrometry—the system Fe-Co-Ni and implications for condensation processes in
630 the solar nebula. Geochim. Cosmochim. Acta, 46(4):549–556.

631 D. J. Frost and C. A. McCammon, 2008. The redox state of earth's mantle. Annu. Rev. Earth
632 Planet. Sci., 36:389–420.

633 A. Gargano, Z. Sharp, C. Shearer, J.I. Simon, A. Halliday, W. Buckley, 2020. The Cl isotope
634 composition and halogen contents of Apollo-return samples. Proc. Nat. Acad. Sci.
635 117, 23418-23425.

636 R. B. Georg, A. N. Halliday, E. A. Schauble, and B. C. Reynolds, 2007. Silicon in the Earth's
637 core. Nature, 447(7148):1102–1106.

638 D.H. Green, I.A. Nicholls, M. Viljoen, R. Viljoen, 1975. Experimental demonstration of the
639 existence of peridotitic liquids in earliest Archean magmatism. Geology, 3, 11-14.

J. Guignard, G. Quitté, M. Méheut, M. J. Toplis, F. Poitrasson, D. Connetable, and M. Roskosz, 2020. Nickel isotope fractionation during metal-silicate differentiation of planetesimals: Experimental petrology and ab initio calculations. Geochim. Cosmochim. Acta, 269:238–256.

K.E.J. Hibbert, H.M. Williams, A.C. Kerr, I.S. Putchtel, 2012. Iron isotopes in ancient and modern komatiites: Evidence in support of an oxidised mantle from Archean to present. Earth Planet. Sci. Lett. 321-322, 198-207.

R. C. Hin, C. Burkhardt, M. W. Schmidt, B. Bourdon, and T. Kleine, 2013. Experimental evidence for Mo isotope fractionation between metal and silicate liquids. Earth Planet. Sci. Lett., 379:38–48.

R. C. Hin, C. Fitoussi, M. W. Schmidt, and B. Bourdon, 2014. Experimental determination of the Si isotope fractionation factor between liquid metal and liquid silicate. Earth Planet. Sci. Lett., 387:55–66.

R. C. Hin, M. W. Schmidt, and B. Bourdon, 2012. Experimental evidence for the absence of iron isotope fractionation between metal and silicate liquids at 1 GPa and 1250–1300 °C and its cosmochemical consequences. Geochim. Cosmochim. Acta, 93:164–181.

D. Huang and J. Badro, 2018. Fe-Ni ideality during core formation on Earth. Am. Mineral., 103(10):1707–1710.

A. P. Kantor, I. Y. Kantor, A. V. Kurnosov, A. Y. Kuznetsov, N. A. Dubrovinskaia, M. Krisch, A. A. Bossak, V. P. Dmitriev, V. S. Urusov, and L. S. Dubrovinsky, 2007. Sound wave velocities of fcc Fe-Ni alloy at high pressure and temperature by mean of inelastic X-ray scattering. Phys. Earth Planet. Inter., 164(1-2):83–89.

C. Kato, F. Moynier, M. C. Valdes, J. K. Dhaliwal, and J. M. Day, 2015. Extensive volatile loss during formation and differentiation of the Moon. Nat. Commun., 6:1–4.

J. Kempl, P. Z. Vroon, E. Zinngrebe, and W. van Westrenen, 2013. Si isotope fractionation between Si-poor metal and silicate melt at pressure-temperature conditions relevant to metal segregation in small planetary bodies. Earth Planet. Sci. Lett., 368:61–68.

E. Kubik, J. Siebert, I. Blanchard, A. Agranier, B. Mahan, F. Moynier, 2021a. Earth's volatile accretion as told by Cd, Bi, Sb and Tl core–mantle distribution. Geochim. Cosmochim. Acta, 306:263–280.

E. Kubik, J. Siebert, B. Mahan, J.B. Creech, I. Blanchard, A. Agranier, S. Shcheka, F. Moynier, 2021b. Tracing Earth's volatile delivery with tin. J. Geophys. Res. Solid Earth, 126, e2021JB022026.

E. Kubik, F. Moynier, M. Paquet, J. Siebert, 2021c. Iron isotopic composition of biological standards relevant to medical and biological applications. Front. Med., 8:696367.

S. van der Laan, Y. Zhang, A. K. Kennedy, and P. J. Wyllie, 1994. Comparison of element and isotope diffusion of K and Ca in multicomponent silicate melts. Earth Planet. Sci. Lett., 123(1-3):155–166.

J. Labidi, A. Shahar, C. Le Losq, V. J. Hillgren, B. O. Mysen, and J. Farquhar, 2016. Experimentally determined sulfur isotope fractionation between metal and silicate and implications for planetary differentiation. Geochim. Cosmochim. Acta, 175:181–194.

C. Lazar, E. D. Young, and C. E. Manning, 2012. Experimental determination of equilibrium nickel isotope fractionation between metal and silicate from 500°C to 950°C. Geochim. Cosmochim. Acta, 86:276–295.

684 C. E. Lesher, 1990. Decoupling of chemical and isotopic exchange during magma mixing.
685 Nature, 344(6263):235–237.

686 C. E. Lesher, J. Dannberg, G. H. Barfod, N. R. Bennett, J. J. Glessner, D. J. Lacks, and J. M.
687 Brenan, 2020. Iron isotope fractionation at the core–mantle boundary by
688 thermodiffusion. Nat. Geosci., 13(5):382–386.

689 J. F. Lin, V. V. Struzhkin, W. Sturhahn, E. Huang, J. Zhao, M. Y. Hu, E. E. Alp, H. kwang
690 Mao, N. Boctor, and R. J. Hemley, 2003. Sound velocities of iron- nickel and iron-
691 silicon alloys at high pressures. Geophys. Res. Lett., 30(21):1–4.

692 J. Liu, N. Dauphas, M. Roskosz, M. Y. Hu, H. Yang, W. Bi, J. Zhao, E. E. Alp, J. Y. Hu, and
693 J. F. Lin, 2017. Iron isotopic fractionation between silicate mantle and metallic core at
694 high pressure. Nat. Commun., 8:1–6.

695 Y. Liu, M. J. Spicuzza, P. R. Craddock, J. M. Day, J. W. Valley, N. Dauphas, and L. A.
696 Taylor, 2010. Oxygen and iron isotope constraints on near-surface fractionation effects
697 and the composition of lunar mare basalt source regions. Geochim. Cosmochim. Acta,
698 74(21):6249–6262.

699 B. Mahan, J. Siebert, E. A. Pringle, and F. Moynier, 2017. Elemental partitioning and isotopic
700 fractionation of Zn between metal and silicate and geochemical estimation of the S
701 content of the Earth's core. Geochim. Cosmochim. Acta, 196:252–270.

702 B. Martorell, J. Brodholt, I. G. Wood, and L. Vočadlo, 2013. The effect of nickel on the
703 properties of iron at the conditions of Earth's inner core: Ab initio calculations of
704 seismic wave velocities of Fe-Ni alloys. Earth Planet. Sci. Lett., 365:143–151.

705 V. Matjuschkin, R.A. Brooker, B. Tattitch, J.D. Blundy, C.C. Stamper, 2015. Control and
706 monitoring of oxygen fugacity in piston cylinder experiments. Contrib. Mineral.
707 Petrol. 169:9.

708 P. McDade, B. Wood, W. Van Westrenen, R. Brooker, G. Gudmundsson, H. Soulard, J.
709 Najorka, and J. Blundy, 2002. Pressure corrections for a selection of piston-cylinder
710 cell assemblies. Mineral. Mag., 66(6):1021–1028.

711 F. Moynier, Q. Z. Yin, and E. Schauble, 2011. Isotopic evidence of Cr partitioning into
712 Earth's core. Science, 331(6023):1417–1420.

713 O. Nebel, P. A. Sossi, J. Foden, A. Bénard, P. A. Brandl, J. A. Stammeier, J. Lupton, M.
714 Richter, and R. J. Arculus, 2018. Iron isotope variability in ocean floor lavas and
715 mantle sources in the Lau back-arc basin. Geochim. Cosmochim. Acta, 241:150–163.

716 A. Néri, M. Monnereau, J. Guignard, M. Bystricky, C. Tenailleau, B. Duployer, M.J. Toplis,
717 G. Quitté, 2021. Textural evolution of metallic phases in a convecting magma ocean:
718 A 3D microtomography study. Phys. Earth Planet. Int., 319:106771.

719 P. Ni, N.L. Chabot, C.J. Ryan, A. Shahar, 2020. Heavy iron isotope composition of iron
720 meteorites explained by core crystallization. Nat. Geosci. 13, 611-615.

721 R. A. Oriani, 1953. Thermodynamic activities in iron-nickel alloys. Acta metall., 1(4):448–
722 454.

723 H. Palme, H. O'Neill, 2014. Cosmochemical estimates of mantle composition. Planets,
724 asteroids, comets and the solar system, volume 2 of Treatise on Geochemistry. Edited
725 by Andrew M. Davis, 149–211.

726 D. Perkins and R. Newton, 1981. Charnockite geobarometers based on coexisting gar- net—
727 pyroxene—plagioclase—quartz. Nature, 292(5819):144–146.

C. Pinilla, A. de Moya, S. Rabin, G. Morard, M. Roskosz, M. Blanchard, 2021. First-principles investigation of equilibrium iron isotope fractionation in $Fe_{1-x}S_x$ alloys at Earth's core formation conditions. Earth Planet. Sci. Lett., 569, 117059.

F. Poitrasson, 2007. Does planetary differentiation really fractionate iron isotopes? Earth Planet. Sci. Lett., 256(3-4):484–492.

F. Poitrasson, A. N. Halliday, D. C. Lee, S. Levasseur, and N. Teutsch, 2004. Iron isotope differences between Earth, Moon, Mars and Vesta as possible records of contrasted accretion mechanisms. Earth Planet. Sci. Lett., 223(3-4):253–266.

F. Poitrasson, M. Roskosz, and A. Corgne, 2009. No iron isotope fractionation between molten alloys and silicate melt to 2000 °C and 7.7 GPa: Experimental evidence and implications for planetary differentiation and accretion. Earth Planet. Sci. Lett., 278(3-4):376–385.

F. Poitrasson, T. Zambardi, T. Magna, and C. R. Neal, 2019. A reassessment of the iron isotope composition of the Moon and its implications for the accretion and differentiation of terrestrial planets. Geochim. Cosmochim. Acta, 267:257–274.

V. B. Polyakov, 2009. Equilibrium iron isotope fractionation at core-mantle boundary conditions. Science, 323(5916):912–914.

E. A. Pringle and F. Moynier, 2017. Rubidium isotopic composition of the Earth, mete- orites, and the Moon: Evidence for the origin of volatile loss during planetary accretion. Earth Planet. Sci. Lett., 473:62–70.

K. Righter and M. J. Drake, 1996. Core formation in Earth's moon, Mars, and Vesta. Icarus, 124(2):513–529.

P. Savage, F. Moynier, H. Chen, G. Shofner, J. Siebert, J. Badro, and I. Puchtel, 2015. Copper isotope evidence for large-scale sulphide fractionation during Earth's differen- tiation. Geochemical Perspect. Lett., pages 53–64.

R. Schoenberg and F. von Blanckenburg, 2006. Modes of planetary-scale Fe isotope fractionation. Earth Planet. Sci. Lett., 252(3-4):342–359.

A. Shahar, V. J. Hillgren, E. D. Young, Y. Fei, C. A. Macris, and L. Deng, 2011. High-temperature Si isotope fractionation between iron metal and silicate. Geochim. Cosmochim. Acta, 75(23):7688–7697.

A. Shahar and E. D. Young, 2020. An assessment of iron isotope fractionation during core formation. Chem. Geol., 554:119800.

A. Shahar, E. D. Young, and C. E. Manning, 2008. Equilibrium high-temperature Fe iso- tope fractionation between fayalite and magnetite: An experimental calibration. Earth Planet. Sci. Lett., 268(3-4):330–338.

A. Shahar, K. Ziegler, E. D. Young, A. Ricolleau, E. A. Schauble, and Y. Fei, 2009. Experimentally determined Si isotope fractionation between silicate and Fe metal and implications for Earth's core formation. Earth Planet. Sci. Lett., 288(1-2):228–234.

Z. D. Sharp, C. K. Shearer, K. D. McKeegan, J. D. Barnes, and Y. Q. Wang, 2010. The Chlorine Isotope Composition of the Moon and Implications for an Anhydrous Mantle. Science, 329(5995):1050–1053.

J. Siebert, A. Corgne, and F. J. Ryerson, 2011. Systematics of metal-silicate partitioning for many siderophile elements applied to Earth's core formation. Geochim. Cosmochim. Acta, 75(6):1451–1489.

E.M. Smith, P. Ni, S.B. Shirey, S.H. Richardson, W. Wang, A. Shahar, 2021. Heavy iron in large gem diamonds traces deep subduction of serpentinized ocean floor. Sci. Adv., 7, eabe9773.

C.R. Soderman, S. Matthews, O. Shorttle, M.G. Jackson, S. Ruttor, O. Nebel, S. Turner, C. Beier, M.A. Millet, E. Widom, M. Humayun, H. Williams, 2021. Heavy δ^{57}Fe in ocean island basalts: A non-unique signature of processes and source lithologies in the mantle. Geochim. Cosmochim. Acta, 292, 309-332.

P. A. Sossi, G. P. Halverson, O. Nebel, and S. M. Eggins, 2015. Combined separation of Cu, Fe and Zn from rock matrices and improved analytical protocols for stable isotope determination. Geostand. Geoanalytical Res., 39(2):129–149.

P. A. Sossi and F. Moynier, 2017. Chemical and isotopic kinship of iron in the Earth and Moon deduced from the lunar Mg-Suite. Earth Planet. Sci. Lett., 471:125–135.

P. A. Sossi, O. Nebel, M. Anand, and F. Poitrasson, 2016a. On the iron isotope composition of Mars and volatile depletion in the terrestrial planets. Earth Planet. Sci. Lett., 449:360–371.

P. A. Sossi, F. Moynier, and K. Van Zuilen, 2018a. Volatile loss following cooling and accretion of the Moon revealed by chromium isotopes. Proc. Natl. Acad. Sci. U. S. A., 115(43):10920–10925.

P. A. Sossi, O. Nebel, and J. Foden, 2016b. Iron isotope systematics in planetary reservoirs. Earth Planet. Sci. Lett., 452:295–308.

P. A. Sossi, O. Nebel, H. S. C. O'Neill, and F. Moynier, 2018b. Zinc isotope composition of the Earth and its behaviour during planetary accretion. Chem. Geol., 477:73–84.

P.A. Sossi, H.S.C. O'Neill, 2017. The effect of bonding environment on iron isotope fractionation between minerals at high temperature. Geochim. Cosmochim. Acta, 196:121–141.

L.J. Swartzendruber, V.P. Itkin, C.B. Alcock, 1991. The Fe-Ni (iron-nickel) system. J. Phase Equilib., 12:288–312.

F.Z. Teng, N. Dauphas, S. Huang, B. Marty, 2013. Iron isotopic systematics of oceanic basalts. Geochim. Cosmochim. Acta, 107, 12-26.

Y. Thibault and M. J. Walter, 1995. The influence of pressure and temperature on the metal-silicate partition coefficients of nickel and cobalt in a model C1 chondrite and implications for metal segregation in a deep magma ocean. Geochim. Cosmochim. Acta, 59(5):991–1002.

H. C. Urey, 1947. The thermodynamic properties of isotopic substances. J. Chem. Soc., pages 562–581.

T. Wakamatsu, K. Ohta, T. Yagi, K. Hirose, and Y. Ohishi, 2018. Measurements of sound velocity in iron–nickel alloys by femtosecond laser pulses in a diamond anvil cell. Phys. Chem. Miner., 45(6):589–595.

K. Wang and S. B. Jacobsen, 2016. Potassium isotopic evidence for a high-energy giant impact origin of the Moon. Nature, 538(7626):487–490.

K. Wang, S. B. Jacobsen, F. Sedaghatpour, H. Chen, and R. L. Korotev, 2015. The earliest Lunar Magma Ocean differentiation recorded in Fe isotopes. Earth Planet. Sci. Lett., 430:202–208.

K. Wang, F. Moynier, J.A. Barrat, B. Zanda, R.C. Paniello, P.S. Savage, 2013. Homogeneous distribution of Fe isotopes in the early solar nebula. Meteorit. Planet, Sci., 48, 354-364.

K. Wang, F. Moynier, N. Dauphas, J. A. Barrat, P. Craddock, and C. K. Sio, 2012. Iron isotope fractionation in planetary crusts. Geochim. Cosmochim. Acta, 89:31–45.

K. Wang, P.S. Savage, F. Moynier, 2014. The iron isotope composition of enstatite meteorites: Implications for their origin and the metal/sulfide Fe isotopic fractionation factor. Geochim. Cosmochim. Acta, 142, 149-165.

X. Wang, C. Fitoussi, B. Bourdon, B. Fegley, S. Charnoz, 2019. Tin isotopes indicative of liquid-vapour equilibration and separation in the Moon-forming disk. Nat. Geo., 12:707–711.

Y. Waseda, M. Ohtani, 1974. Static structure of liquid noble and transition metals by X-ray diffraction. Physica status solidi (b), 62:535–546.

S. Weyer, A. D. Anbar, G. P. Brey, C. Münker, K. Mezger, and A. B. Woodland, 2005. Iron isotope fractionation during planetary differentiation. Earth Planet. Sci. Lett., 240(2):251–264.

S. Weyer, D.A. Ionov, 2007. Partial melting and melt percolation in the mantle: The message from Fe isotopes. Earth Planet. Sci. Lett., 259, 119-133.

H. M. Williams, A. Markowski, G. Quitté, A.N. Halliday, N. Teutsch, S. Levasseur, 2006. Fe isotope fractionation in iron meteorites: New insights into metal-sulphide segregation and planetary accretion. Earth Planet. Sci. Lett. 250, 486-500.

H. M. Williams, B. J. Wood, J. Wade, D. J. Frost, and J. Tuff, 2012. Isotopic evidence for internal oxidation of the Earth's mantle during accretion. Earth Planet. Sci. Lett., 321-322:54–63.

J. Wimpenny, L. Borg, C.K. Sio, 2022. The gallium isotopic composition of the Moon. Earth Planet. Sci. Lett., 578:117318.

B. J. Wood, M. J. Walter, and J. Wade, 2006. Accretion of the Earth and segregation of its core. Nature, 441(7095):825–833.

B.J. Wood, D.J. Smythe, T. Harrison, 2019. The condensation temperature of the elements: A reappraisal. American Mineralogist, 104:844–856.

Y. Xia, E. Kiseeva, J. Wade, and F. Huang, 2019. The effect of core segregation on the Cu and Zn isotope composition of the silicate Moon. Geochemical Perspect. Lett., pages 12–17.

H. Yang, J.F. Lin, M.Y. Hu, M. Roskosz, W. Bi, J. Zhao, E.E. Alp, J. Liu, J. Liu, R.M. Wentzcovitch, T. Okuchi, N. Dauphas, 2019. Iron isotopic fractionation in mineral phases from Earth's lower mantle: Did terrestrial magma ocean crystallization fractionate iron isotopes? Earth Planet. Sci. Lett. 506, 113-122.

E.D. Young, 2021. Revisiting the Wasson fractional crystallization model for IIIAB iron meteorites with implications for the interpretation of their Fe isotope ratios. Meteorit. Planet. Sci. 1-10.

G. Zellars, S. Payne, J. Morris, and R. Kipp, 1959. The activities of iron and nickel in liquid Fe-Ni alloys. Trans. Metall. Soc., 215:181–185.

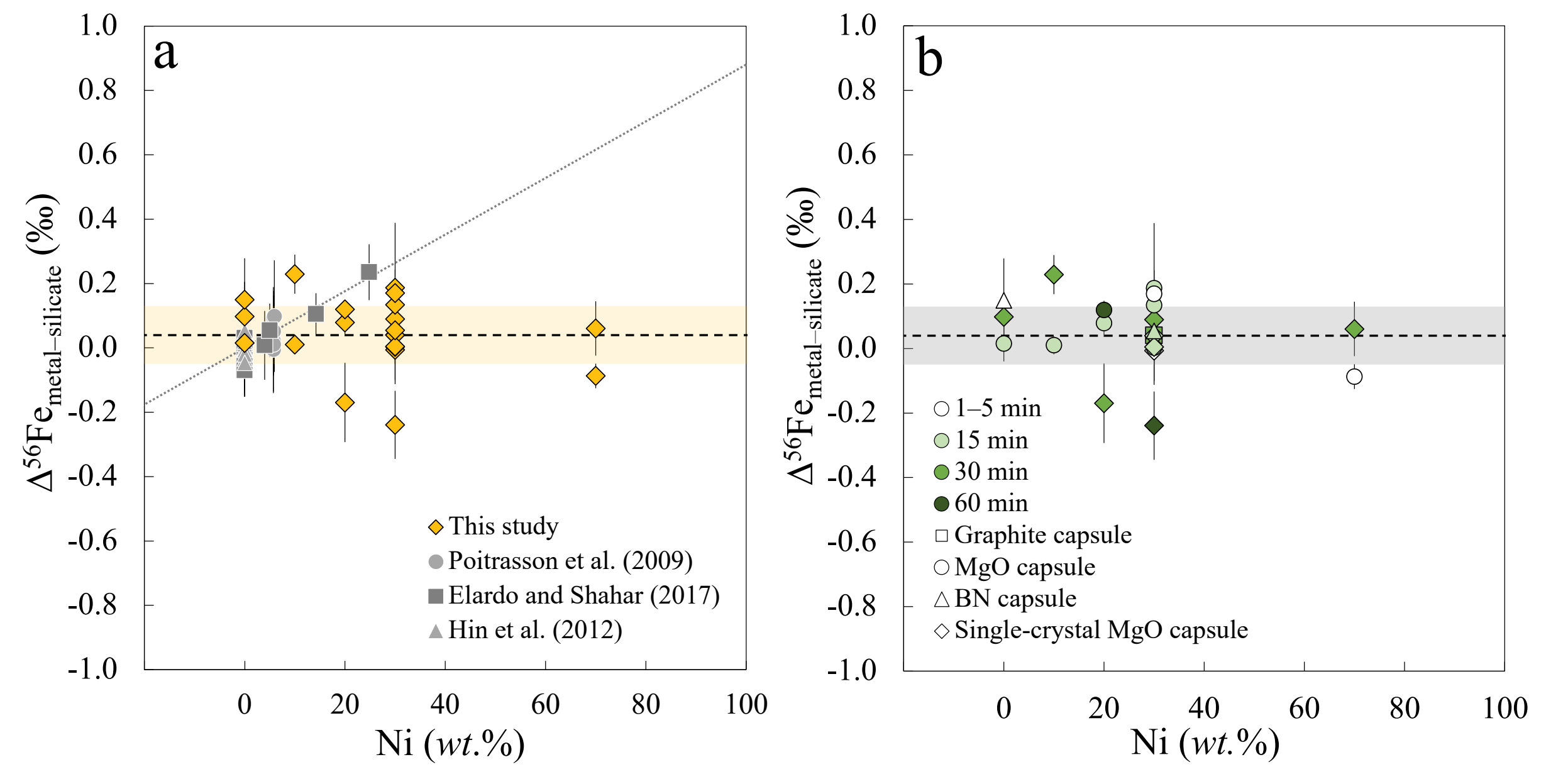
a
b
1.0
0.8
0.6
0.4
0.2
0.0
-0.2
-0.4
-0.6
-0.8
-1.0
$\Delta^{56}Fe_{metal-silicate}$ (‰)
0
20
40
60
80
100
Ni (*wt.*%)
This study
Poitrasson et al. (2009)
Elardo and Shahar (2017)
Hin et al. (2012)
1–5 min
15 min
30 min
60 min
Graphite capsule
MgO capsule
BN capsule
Single-crystal MgO capsule

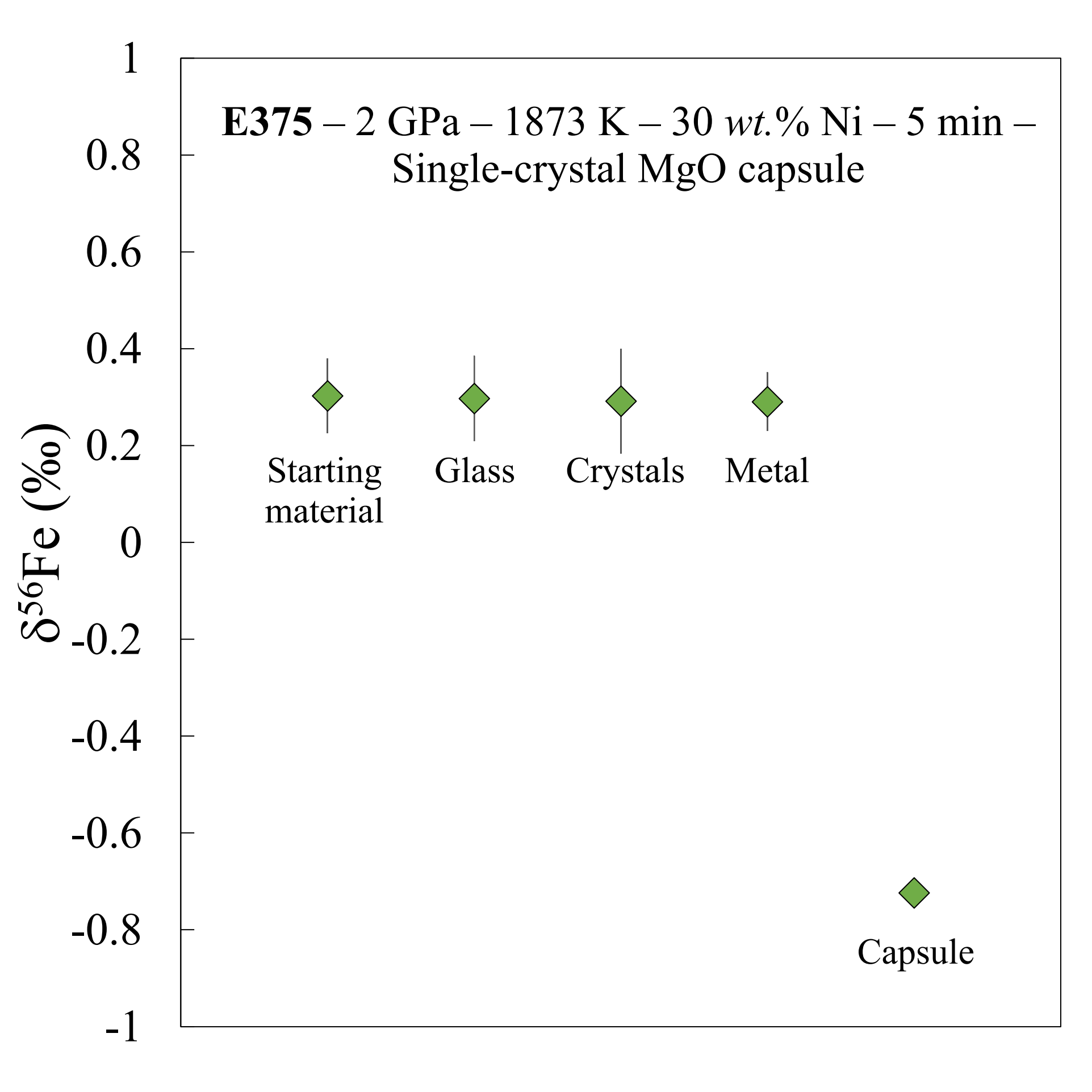
E375 – 2 GPa – 1873 K – 30 *wt.*% Ni – 5 min –
Single-crystal MgO capsule
δ^{56}Fe (‰)
1
0.8
0.6
0.4
0.2
0
-0.2
-0.4
-0.6
-0.8
-1
Starting material
Glass
Crystals
Metal
Capsule

$\equiv |\Delta^{56}Fe_{metal-silicate}| > 0.06$ ‰

□ Graphite capsule

○ MgO capsule

△ BN capsule

◇ Single-crystal MgO capsule

○ 1–5 min

○ 15 min

● 30 min

● 60 min

$$\delta^{56}Fe_{final\ bulk} = \frac{\delta^{56}Fe_{sil} \cdot f_{sil} \cdot X_{sil}^{Fe} + \delta^{56}Fe_{met} \cdot f_{met} \cdot X_{met}^{Fe}}{f_{sil} \cdot X_{sil}^{Fe} + f_{met} \cdot X_{met}^{Fe}}$$

$\delta^{56}Fe_{bulk}$ (‰)

1.0
0.9
0.8
0.7
0.6
0.5
0.4
0.3
0.2
0.1
0.0

Fe dopant

Initial bulk (starting material)

MORB

0% Ni
10% Ni
20% Ni
30% Ni
70% Ni

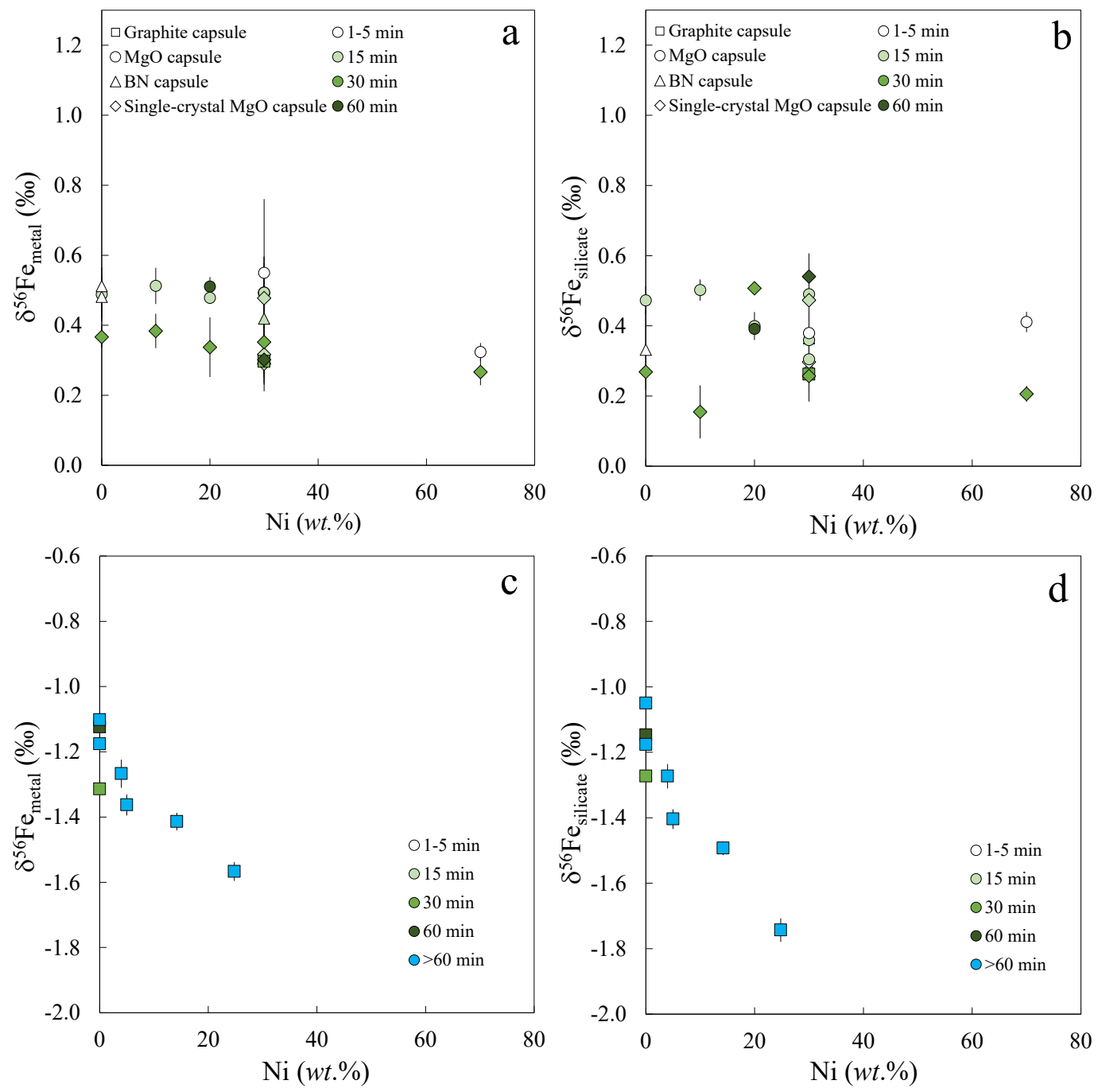
a
b
c
d
Graphite capsule
MgO capsule
BN capsule
Single-crystal MgO capsule
1-5 min
15 min
30 min
60 min
>60 min
δ56Fe metal (‰)
δ56Fe silicate (‰)
Ni (wt.%)
0.0
0.2
0.4
0.6
0.8
1.0
1.2
-0.6
-0.8
-1.0
-1.2
-1.4
-1.6
-1.8
-2.0
0
20
40
60
80